Lasers in Manufacturing and Materials Processing (2026) 13:555–581
https://doi.org/10.1007/s40516-026-00347-7

RESEARCH

Laser 3D-printed Periodic Porous Structures for Heat Exchangers: A Novel Characterization Approach Under Fully Developed Conditions

Samuele Piandoro[1] · Filippo Azzini[1] · Michele Francioso[1] · Dexiang Zha[1] · Erica Liverani[1] · Beatrice Pulvirenti[1] · Alessandro Fortunato[1]

Received: 2 September 2025 / Revised: 11 February 2026 / Accepted: 2 May 2026 /
Published online: 19 May 2026

Abstract

Triply Periodic Minimal Surfaces (TPMS) have garnered significant attention in recent years because of their potential for enhancing heat transfer performance. Recent advances in additive manufacturing have made it possible to fabricate these complex geometries; however, accurately characterizing their thermal-hydraulic performance remains challenging. To address this, this paper proposes a novel approach leveraging periodic boundary conditions to simulate fully developed flow and heat transfer within TPMS, eliminating inlet/outlet effects to focus on the structure's core region. The methodology was validated against experimental literature, showing excellent agreement in Nusselt number predictions. A case study on gyroid-based heat exchangers investigated the impact of edge dimension and wall thickness on performance. Key findings reveal that the Performance Evaluation Criterion (PEC) increases with porosity, with all designs exceeding the efficiency of traditional smooth ducts (PEC > 1). Specifically, gyroids with 45–50% porosity were identified as optimal, achieving a maximum PEC of 6.5 while strictly satisfying Laser Powder Bed Fusion (LPBF) printability constraints (minimum channel diameter $> \mathbf{1.2}$ mm). Furthermore, a simplified correlation between the Nusselt and Forchheimer numbers is proposed to streamline future design optimizations. By providing a rigorous framework for characterization, this work enables the development of highly efficient and innovative thermal management solutions.

Keywords Triply periodic minimal surface · Laser additive manufacturing · Numerical characterization · Fully developed condition · Darcy law

Filippo Azzini and Samuele Piandoro contributed equally to this work.

Extended author information available on the last page of the article

Introduction

The increasing demand for advanced heat exchangers spans various industries due to the critical need for effective thermal management solutions. Fields such as automotive, aerospace, renewable energy, data centers, and electronics depend on efficient heat dissipation to ensure system reliability, optimal performance, and extended lifespans [1, 2]. As global electricity generation is projected to increase substantially, reaching 31,297 TWh by 2050 [3], the necessity for effective thermal management solutions becomes even more pressing. Conventional heat dissipation methods, which often depend on bulky heat sinks and traditional manufacturing processes, fall short of meeting the requirements of modern compact systems [4]. Traditional manufacturing techniques, such as milling, shearing, drilling, casting, and forming, are predominantly based on material removal, leading to significant environmental and energy costs [5]. Additive Manufacturing (AM) has introduced new possibilities for creating compact and efficient heat exchanger structures [6, 7], while also offering the benefit of a reduced environmental impact [8]. Over the past few decades, AM has expanded to include several techniques such as Selective Laser Powder Bed Fusion (LPBF), Direct Energy Deposition (DED), and Wire Arc Manufacturing (WAM) [9]. These processes provide distinct advantages over traditional methods, including greater design flexibility, improved material utilization, faster production times, and cost efficiency over time. By constructing components layer by layer from a digital design, AM allows the fabrication of intricate geometries that are often unachievable with conventional methods, while also reducing material waste. Complex internal structures, organic forms, and lightweight but durable designs can be created, enabling customization for specific performance requirements. This capability has led to the development of heat exchangers with intricate geometries that improve heat transfer efficiency and thermal performance. Among the innovative geometries for heat exchangers, lattice-based structures derived from triply periodic minimal surfaces (TPMS) have emerged as highly promising [10, 11]. Unlike other advanced structures like metal foams, TPMS geometries are defined by mathematical equations, allowing precise control over their properties and configurations [12]. These structures possess a range of beneficial properties, including a high stiffness-to-weight ratio, a large surface-area-to-volume ratio, and exceptional mechanical energy absorption. Such characteristics make TPMS geometries valuable in diverse applications, including aerospace [13], automotive [14], and thermal management. Given the adaptability of TPMS structures, optimizing their geometry for specific applications prior to manufacturing is critical. Instead of relying solely on experimental approaches to explore various configurations, Computer-Aided Engineering (CAE) tools enable the efficient design and analysis of TPMS geometries. Software such as nTop, SolidWorks, ANSYS, and open-source platforms like TPMS Designer [15] facilitate precise evaluation of their mechanical and thermal properties. This computational strategy accelerates the design process, allowing for fine-tuning of TPMS structures to meet application-specific requirements. Numerous studies have investigated the use of Computational Fluid Dynamics (CFD) for optimizing heat exchanger designs incorporating TPMS geometries. For example, Pulvirenti et al. [11] examined the fluid dynamics and heat transfer characteristics

of a gyroid-based TPMS structure. Similarly, Khalil et al. [16] analyzed forced convection within three periodically arranged TPMS structures using both numerical and experimental methods. Wang [17] assessed the thermal-hydraulic performance of TPMS channels with varying cell volume fractions, while Baobaid [18] explored free convection heat transfer in TPMS structures, particularly gyroid and diamond configurations, under bottom-heated conditions. In the context of forced convection with anti-freezing fluids, Saghir et al. [19] performed a combined experimental and numerical investigation on aluminum Gyroid structures using an ethylen glycol/water mixture. Conventional approaches to characterizing TPMS structures often simulate a limited number of unit cells with inlet and outlet regions. In such studies, a defined flow rate is applied at the inlet while the outlet is subjected to constant pressure. The TPMS is then exposed to either a constant temperature or a heat flux. However, the inclusion of inlet and outlet regions can influence the results significantly, as shown in studies by Dukhan et al. [20] and Baril et al. [21], who examined entrance and exit effects in fluid flow through porous media. Their findings emphasized the need for a critical length of porous media to minimize such influences. To address these challenges, this paper presents a novel methodology employing periodic boundary conditions to simulate the hypothetical infinite repetition of elementary TPMS cells, thereby achieving fully developed flow. Under these conditions, the hydraulic performance, characterized by permeability and the form drag coefficient, depends solely on the TPMS geometry and the dimensionless Reynolds number. This approach is rooted in the Darcy-Forchheimer equation, a widely accepted model for fluid motion in porous media [22]. The proposed method also facilitates the attainment of a fully developed thermal state, where the Reynolds number and geometry are the primary determinants of the Nusselt number. By combining these parameters, Performance Evaluation Criterion (PEC) can be derived, offering a standardized metric for assessing the efficiency of TPMS geometries, with values above 1 indicating enhanced performance compared to traditional cases. This methodology is detailed in this study and applied to compare various cell geometries at equivalent Reynolds numbers. The approach is demonstrated through a case study involving a gyroid structure with ethylene glycol as the working fluid. Parameters such as cell edge dimensions and wall thickness are varied to assess their effects on thermal and hydraulic performance, as well as printability. Furthermore, the reliability of the proposed numerical framework is rigorously validated through a comparison with contemporary experimental data reported by Saghir et al. [19].

Materials and Methods

This section presents the methodology used for the proposed approach, and later, a case study. In Section "TPMS Definition", the definition of TPMS structures is presented with the geometric parameters involved in the evaluation of cells. Section "Proposed Approach" describes the fluid dynamics and thermal models used for the analysis, while the case study and the LPBF benchmark are illustrated in Section "Gyroid Case Study and LPBF Benchmarking". Finally, a numerical implementation

of the approach is shown in Section "Numerical Implementation" using commercially available software.

TPMS Definition

Triply Periodic Minimal Surfaces (TPMS) are mathematically defined as minimal surfaces that can be fully represented in three dimensions and have translational and rotational symmetries along all three axes; for this reason, they can be unequivocally described starting from implicit equations [23]. One of the most used TPMS structures, which will be later investigated, is the gyroid, depicted in Fig. 1 and based on the Eq. 1:

$$sin(\omega_x x)cos(\omega_y y) + sin(\omega_z z)cos(\omega_x x) + sin(\omega_y y)cos(\omega_z z) = H \tag{1}$$

Where parameters ω_x, ω_y, and ω_z represent the periodicity along the Cartesian directions (x, y, and z), while H is the offset. When H = 0, the result is a flat surface that divides the space in two volumes, whereas setting $H \neq 0$ generates a sheet with a thickness equal to 2H. The structure of the TPMS unit cell can be implicitly designed and generated using the software nTop [24], specifying the following parameters: edge length and wall thickness (t_w) in Fig. 1. Fixing the edge length and the wall thickness makes it possible to unequivocally obtain two derived quantities that have a strong correlation with the hydraulic and thermal performance of the cell. The minimum channel diameter (ϕ_{min}) is defined by a transversal section located in the diagonal plane of the TPMS cell, as shown in Fig. 1. The other commonly used properties are the porosity (φ) defined as the ratio between the volume occupied by the void inside the cell (V_f) and the total volume, i.e., the sum of the fluid and the solid (V_s):

$$\varphi = \frac{V_f}{V_f + V_s} \tag{2}$$

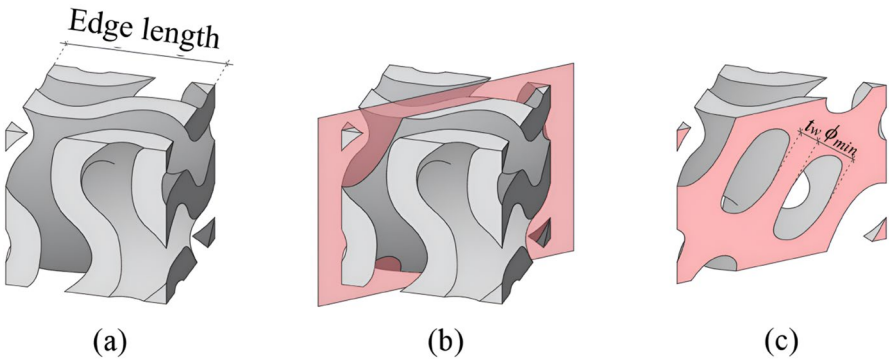

Fig. 1 Geometric definition of TPMS structure with **a**) Elementary cell with edge length, **b**) transversal cutting plane and **c**) wall thickness (t_w) and minimum channel diameter (ϕ_{min}) showed in the section

At a fixed edge length, increasing the wall thickness leads to a reduction in both φ and ϕ_{min}, eventually resulting in complete channel obstruction. Therefore, for each cell dimension, a maximum wall thickness can be defined as the largest value that still keeps the channel open.

Proposed Approach

The fluid flow inside the TPMS structure is governed by the laminar Navier-Stokes equations, the conservation of mass (Eq. 3):

$$\nabla \cdot (\rho \vec{v}) = 0 \tag{3}$$

and the conservation of momentum (Eq. 4):

$$\nabla \cdot (\rho \vec{v} \otimes \vec{v}) = \nabla \cdot \sigma + \vec{f_b} \tag{4}$$

Where ρ is the density, $\vec{v}$ is the velocity vector field, σ is the stress tensor and $\vec{f_b}$ is the resultant of all the body forces per unit volume acting on the continuum. Traditional approaches used to characterize porous medium use the superficial velocity (also referred to as Darcy velocity), however, since we are interested in characterizing the unit cell, and in the proposed approach the fluid remains inside the TPMS channels without any inlet and outlet expansion, the intrinsic velocity was considered as more suitable and therefore will be the only one considered, similarly to other studies [25]. However, the conversion can be easily made by multiplying the intrinsic velocity by the cell's porosity value. The minimum channel diameter, as defined in Section "TPMS Definition", can be used to calculate the dimensionless quantities typically used to characterize hydraulic and thermal performance, starting from the Reynolds number (Eq. 5):

$$Re_{\phi_{min}} = \frac{\rho \|\vec{v}\| \phi_{min}}{\mu} \tag{5}$$

Where μ is the fluid viscosity. Considering an infinite series of periodic elementary cells, sufficiently distant from the initial and final cells, the velocity field is not influenced by the inlet and outlet regions. In that condition, the velocity profile at any scaled x/L position depends only on the mass flow rate (and therefore the Reynolds number) and the geometry of the elementary cell itself. Additionally, the pressure drop normalized by the channel length is not affected by the number of cells taken into account. The momentum transfer model for fluid inside porous media, based on Darcy's law and its extensions [26], can be used to characterize any TPMS structure.

$$\frac{\mu}{K} \vec{v} = -\nabla p + \rho \vec{g} \tag{6}$$

where K is the permeability of the porous medium and indicates the ability for fluids to flow through it. It is measured in m^2 or more typically in Darcy (d), where 1 Darcy

is roughly equivalent to $10^{-12}\mathrm{m}^2$. Experimental investigations have shown that this linear correlation between velocity and pressure drop holds only in the creeping flow condition, when the viscous forces dominate over the inertial one. Indeed, by increasing the mass flow rate, the correlation diverges and becomes more like a quadratic one [27]. This transition can be expressed by the Hazen-Dupuit-Darcy, or simply the Darcy-Forchheimer, equation (Eq. 7):

$$\frac{\mu}{K}\vec{v}\left(1+c_F\frac{\rho_f\sqrt{K}\|\vec{v}\|}{\mu}\right)=-\nabla p+\rho\vec{g} \tag{7}$$

Where c_F is a dimensionless property called inertial, or form-drag, coefficient, and is related to the geometry of the porous media. Assuming that the fluid flow is directed toward the x-axis and neglecting the gravity force, the equation can be rearranged to highlight the contribution of two terms; the inertial and the viscous one (Eq. 8)

$$-\frac{dp}{dx}=\frac{\mu}{K}u+\frac{c_F\rho}{\sqrt{K}}u^2=R_v u+R_i u^2 \tag{8}$$

By fitting the normalized pressure drop against the intrinsic velocity with a quadratic curve the two coefficients R_v and R_i can be obtained and used to determine K and c_F . These two coefficients can be used inside the body forces in Eq. 4 as a momentum source [26]. This would avoid the explicit definition and generation of the porous medium as the momentum source term would contribute to the pressure gradient in the domain, creating a pressure drop proportional to the fluid velocity. The Darcy friction factor is ultimately calculated with Eq. 9 to quantify the hydraulic resistance given by each TPMS elementary cell:

$$f=\frac{2\Delta P\phi_{min}}{L\rho u^2} \tag{9}$$

Similarly, the thermal behavior of the elementary cell can be evaluated by solving the energy equation for both the fluid inside the TPMS and the metal region by using Eq. 10 for the former and Eq. 11 for the latter:

$$\nabla\cdot(\rho E\vec{v})=\nabla\cdot(\vec{v}\cdot\sigma)-\nabla\cdot\vec{q}+S_{gen} \tag{10}$$

$$\nabla^2 T=0 \tag{11}$$

Where E is the total energy per unit mass, $\bar{q}$ is the heat flux and S_{gen} is the energy source per unit volume. The first term on the right-hand side of Eq. 10 ($\nabla\cdot(\vec{v}\cdot\sigma)$) represents the viscous dissipation term. At the low Reynolds numbers considered in the latter case study it has a negligible impact on the overall energy balance. As previously mentioned, an infinite channel composed of elementary cell repetition is used to characterize the unitary cell. The temperature field becomes self-similar when it is far enough from the inlet and outlet cells; thus, if an appropriate scaling factor

is used (Eq. 12), the temperature profile at any x/L is independent of the specific cell under consideration.

$$T - T_{inlet} = const \tag{12}$$

This condition can be seen as the equivalent of the fully developed thermal condition in a pipe, where both the bulk and the wall temperature increase linearly [28]. The temperature profile in a TPMS cell varies in a streamwise direction, but it repeats periodically, and it is constant across all cells in each x/L, as for the velocity. The heat transfer coefficient assumes a periodic trend for which an average value can be determined. The dimensionless Nusselt number ($Nu_{\phi_{min}}$) can be introduced, as

$$Nu_{\phi_{min}} = \frac{h\phi_{min}}{\lambda} \tag{13}$$

where λ is the thermal conductivity of the fluid and h is the convective heat transfer coefficient (see Eq. 14).

$$h = \frac{q''}{T_{wall} - T_{bulk}} \tag{14}$$

The bulk temperature is calculated as:

$$T_{bulk} = \frac{1}{UA} \int_A TudA \tag{15}$$

where A is the fluid cross-section surface and U is the average velocity evaluated in the cross-section. The improvement of the cell with respect to a reference case (a plain rectangular duct with the same dimension of the TPMS to compare) was at the end estimated by the Performance Evaluator Criterion (PEC) [29, 30], calculated as

$$\mathrm{PEC} = \frac{Nu/Nu_0}{(f/f_0)^{1/3}} \tag{16}$$

The friction factor f_0 (Eq. 17) and the Nusselt number Nu_0 (equal to 3.09) for this reference case are well known in literature [31].

$$f_0 = \frac{56.9}{Re} \tag{17}$$

Gyroid Case Study and LPBF Benchmarking

A case study was chosen to show the application of the method. Gyroids cells with edge length from 3 to 10 mm with a step of 1 mm, and wall thickness starting from 0.5 mm were generated using nTop. Table 1 summarizes all the elementary cells designed. Each cell was assigned an identifier A_B, with A indicating the cell edge

Table 1 List of all gyroid cells generated using nTop for hydraulic and thermal evaluation

A_B	Edge	t_w	ϕ_{min}	φ [%]	A_B	Edge	t_w	ϕ_{min}	φ [%]
	[mm]	[mm]	[mm]			[mm]	[mm]	[mm]	
30_{05}	3	0.5	0.8	34.35	80_{05}	8	0.5	2.97	75.13
30_{08}		0.8	0.45	44.38	80_{08}		0.8	2.67	60.75
40_{05}	4	0.5	1.2	17.59	80_{10}		1	2.47	51.54
40_{08}		0.8	0.9	57.35	80_{15}		1.5	1.97	30.55
40_{10}		1	0.78	34.76	80_{20}		2	1.36	13.07
40_{12}		1.2	0.42	21.42	80_{25}		2.5	0.67	78.26
50_{05}	5	0.5	1.67	10.22	90_{05}	9	0.5	3.4	65.55
50_{08}		0.8	1.37	65.84	90_{08}		0.8	3.1	57.35
50_{10}		1	1.12	46.26	90_{10}		1	2.9	38.11
50_{15}		1.5	0.35	34.35	90_{15}		1.5	2.4	21.17
60_{05}	6	0.5	2.2	6.57	90_{20}		2	1.8	7.88
60_{08}		0.8	1.8	71.20	90_{25}		2.5	1.2	80.63
60_{10}		1	1.6	54.64	90_{30}		3	0.37	69.36
60_{15}		1.5	1.1	44.38	100_{05}	10	0.5	3.8	61.95
60_{20}		2	0.22	21.23	100_{08}		0.8	3.5	44.38
70_{05}	7	0.5	2.53	4.29	100_{10}		1	3.3	28.19
70_{08}		0.8	2.21	75.13	100_{15}		1.5	2.8	14.85
70_{10}		1	2.03	60.75	100_{20}		2	2.28	4.49
70_{15}		1.5	1.48	51.54	100_{25}		2.5	1.7	82.56
70_{20}		2	0.87	30.55	100_{30}		3	1.02	72.26

Table 2 Powder chemical composition [wt.%]

Al	Si	Mg	Fe	Other
balance	10.6	0.4	0.14	<0.1

length and *B* the wall thickness, both multiplied by 10. For each cell the minimum channel diameter and the porosity were calculated and included in the table.

Despite the nominal ϕ_{min} being defined for avoiding geometric occlusion, the real printed channel could be different due to process errors and defects. The printability of LPBF features defines a realistic constraint in gyroid structure design, making all the gyroids outside this constraint not suitable for actual applications. Cubic samples with edges of 10 mm with open holes of 0.1 – 3 mm in diameter and wall thickness of 0.4 mm to 2 mm were designed and printed to evaluate the dimensional and geometrical LPBF constraints. AlSi10Mg atomized powder, supplied by m4p (m4p material solutions GmbH) with the chemical composition reported in Table 2, was used for the manufacturing of benchmark samples. The powder was spherical with dimensions in the range of 20-63 μm.

The LPBF parts were produced using a SISMA MYSINT300 system in a building platform of 300 mm in diameter. All samples were built in a nitrogen environment with a residual oxygen content $< 0.3\%$ using the process parameters summarized in Table 3.

To prevent cell distortion from thermal residual stress, the samples were heat treated for four hours at 160 °C and then cooled to room temperature. Wall thickness were measured by using a micrometer (Mitutoyo, Digimatic Digital Micrometer

Table 3 LPBF process parameters

Power [W]	Scan speed [mm/s]	Hatch dist. [μm]	Layer thick. [μm]	Spot diam. [μm]	Platform temp. [°C]	Scanning strategy
370 (450 edge)	1700 (2000 edge)	170	30	100	150	5×5 mm rot. chessboard

Table 4 Thermodynamic properties used for simulations for both the fluid (ethylene glycol) and solid (Al alloy) regions

	ρ [kg/m^3]	μ [Pa s]	λ [W/m K]	c_p [J/kg K]
$(CH_2OH)_2$	1116.65	0.0161	0.249	2382
AlSi10Mg	2702	–	237	903

IP65) and the mean value of 5 measurements were used to evaluate dimension. The holes diameters were then analyzed by a digital optical microscope (Keyence VHX-7000), and hole circularity Eq. 18 and aspect ratio Eq. 19 by Fiji ImageJ software [32].

$$\text{Circularity} = \frac{4\pi \text{Area}}{\text{Perimeter}^2} \tag{18}$$

$$\text{Aspect Ratio} = \frac{\phi_{max}}{\phi_{min}} \tag{19}$$

Wall thickness and hole diameter were used for process constraints definition. In particular, a threshold was selected between the nominal and measured geometric parameters (thickness and diameter) of 5% to determine the printing constraints. Together with the hole diameter, the aspect ratio was assessed, taking into account the nearly asymptotic nature of the aspect ratio-diameter trend.

Numerical Implementation

All the geometries analyzed were formed by repeating the elementary cells of Table 1 eight times in the flow direction (x-axis) using nTop software. The gyroids were exported from nTop as an STL file and imported by the CFD software (Star-CCM+) as a surface mesh. The plain rectangular channel embedding the gyroid was used to obtain the two regions. The fluid was obtained by a Boolean subtraction, while the solid region by a Boolean intersection operation. A contact interface between the metal and fluid regions was defined to ensure thermal transfer. The fluid considered was ethylene glycol ($(CH_2OH)_2$) and the metal was an aluminum alloy (AlSi10Mg). The properties of both materials, derived from literature [33, 34] are reported in Table 4.

The volumetric computational grid was obtained using a polyhedral mesh, defined in Section "Mesh Convergence" after a mesh convergence, and the following boundary conditions were imposed (see Fig. 2): i) Fully developed condition in the x direction, fixing the mass flow at one surface and imposing the periodicity at the other one. ii) internal periodic boundary conditions in y and z directions, iii) non-slip and imper-

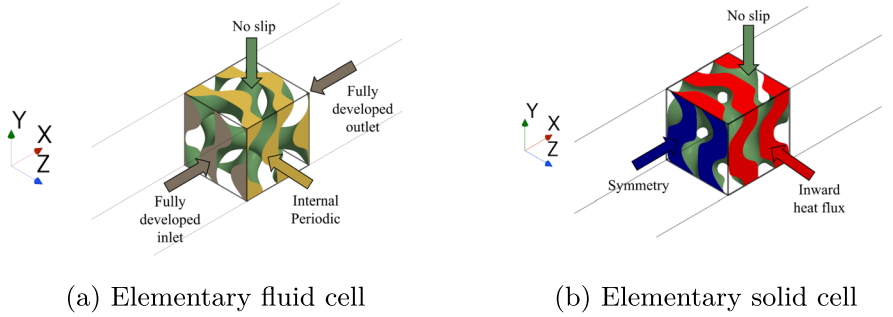

Fig. 2 Boundary condition used for hydraulic and thermal simulations for the fluid (**a**) and solid (**b**) regions

meability wall condition in the contact interface. The fluid flow analysis was carried out to obtain the normalized pressure drop for 10 different velocity magnitudes in the Reynolds range of [1;50] and followed these steps:

1. Calculation of velocity magnitude by imposing the Reynolds number (Eq. 5).
2. Calculation of the mass flow rates by multiplying the gyroid's inlet surface.
3. Solving Eqs. 3 and 4 to obtain pressure and velocity fields inside the domain.
4. Calculation of friction factor (Eq. 9).

After evaluating the hydraulic resistance the thermal performance was evaluated applying the following boundary conditions: i) Symmetry condition in the x direction, ii) fluid internal periodic condition in the y and z surfaces, iii) solid constant inward heat flux in the y and z directions (similarly to [17, 35]). The velocity and pressure fields were imported from the hydraulic simulation and the temperature field was resolved. The Nusselt number (Eq. 13) was evaluated and ultimately the PEC indicator (Eq. 16). An elementary cell is shown for both the fluid region (Fig. 2a) and solid region (Fig. 2b) to better visualize the boundary conditions. In particular the gray surface corresponds to the fully developed condition, in yellow the internal periodic, in green the no slip, in blue the symmetry, and in red the inward heat flux condition.

Two stopping criteria for hydraulic evaluation were chosen, a minimum criterion of $1.0 \cdot 10^{-5}$ for the normalized difference between the imposed mass flow at the inlet and the calculated one at the outlet, and an asymptotic, with at least 250 iterations in the range ± 0.1%, for the pressure drop. Instead, for the thermal evaluation, the Nusselt number was set as the asymptotic stopping criterion with at least 500 iterations in the range of ± 0.1%. The general workflow is summarized in Fig. 3.

Model Validation

To assess the reliability of the proposed computational framework, a validation study was conducted for both hydraulic and thermal predictions. The hydraulic results were verified against the theoretical Darcy-Forchheimer correlation. According to the literature the friction factor can be approximated using the following equation:

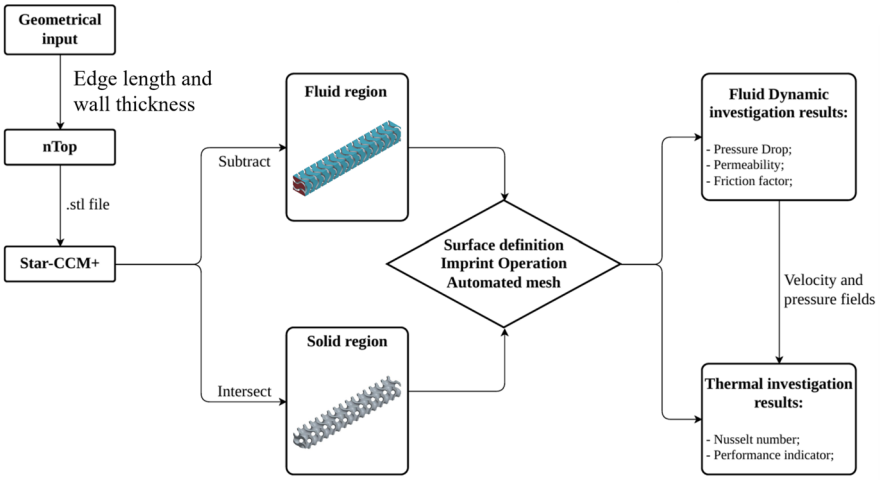

Fig. 3 Workflow: from the generation of the geometrical model in nTop to the setup of the numerical simulations to obtain the hydraulic and thermal characteristic of each cell investigated in Table 1

$$f \approx 1 + \frac{1}{Re_{por}} \tag{20}$$

where Re_{por} is the Reynolds number calculated using the permeability and the form-drag coefficient of the porous media, often called Forchheimer number, given by Eq. 21.

$$Re_{por} = \frac{\rho c_F \sqrt{K} u}{\mu} = \frac{R_i}{R_v} u \tag{21}$$

Regarding the thermal performance, since direct experimental validation of the fully developed condition was not feasible within the scope of this work, the numerical model was validated against the experimental and numerical data recently published by Saghir et al. [19]. The reference study investigated the heat transfer performance of an aluminum gyroid structure using an ethylene glycol/water mixture under a constant heat flux, utilizing a finite-domain approach with inlet and outlet regions. To ensure a consistent comparison, the specific geometric parameters and material properties from the reference were replicated. The Reynolds number was matched based on the hydraulic diameter definition used in the reference study instead of the minimum channel diameter as we proposed. Consequently the comparison between the Nusselt number was performed based on the hydraulic diameter. A comparison between the reference geometry and the proposed approach is shown in Fig. 4 full finite computational domain employed by Saghir et al. (adapted from Figure 7 of Ref. [19]) on the left, contrasted with the present periodic simulation on the right.

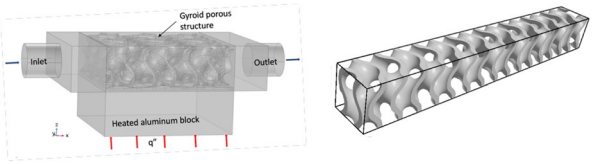

Fig. 4 Thermal validation domain from [19] (left) and extracted domain used within the proposed approach (right)

Table 5 Symbols used for all the graphs in the results section

Edge Dimension [mm]	Symbol
3	●
4	■
5	▲
6	▼
7	◆
8	+
9	×
10	★

Table 6 Gyroids tested for mesh convergence

	Edge length [mm]	Wall thickness [mm]	ϕ_{min} [mm]	φ [%]
High porosity gyroid	10	0.5	3.8	82.5
Low porosity gyroid	6	2	0.22	4.3

Results

In this section, the results of the proposed method are presented and analyzed for the described case study. In order to facilitate the reading of the graphs and avoid repeating the same legend, the symbols shown in Table 5 were used for each previously defined cell dimension (see Table 1) as point markers.

Fluid Dynamics Simulations

Mesh Convergence

A mesh-independent study was conducted to find the best setting for the fluid region's computational grid. Two gyroids differing in their porosity value, with geometric characteristics described in Table 6 were tested. The grid element dimensions were studied in the range between ϕ_{min} (maximum size tested) and 5% of ϕ_{min} (minimum size tested).

For each mesh, the pressure drop and the Nusselt number were calculated at a constant inlet velocity. The results were then analyzed using the minimum mesh size as a reference for both indexes and calculating the percentage difference relative to this value. The results are shown in Fig. 5, in the x-axis are indicated both the mesh cell size (in percentage of the minimum channel diameter) and the total cell generated. The left y-axis refers to the pressure drop relative error, plotted as a dashed line with circle markers, while the right y-axis refers to the Nusselt number relative error,

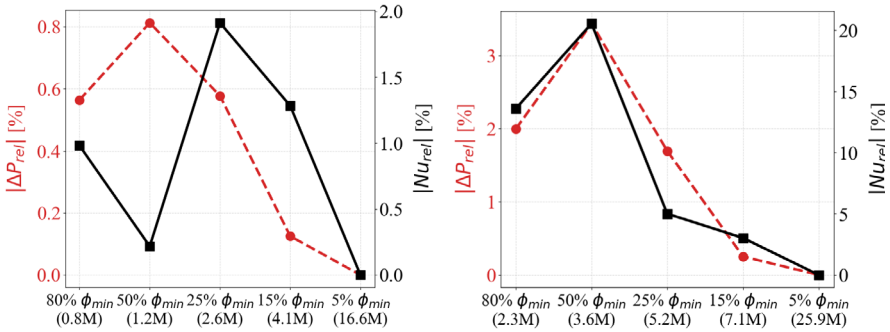

(a) High porosity (b) Low porosity

Fig. 5 Mesh independence study, the pressure drop difference is calculated with reference to the lowest mesh dimension considered

shown as a continuous line with square markers. The pressure drop difference in the high porosity gyroid (Fig. 5a) was almost independent of element number and size (the maximum relative error was less than 1% for all the cases), while the solution is significantly more dependent on mesh size in the case of a low porosity gyroid (Fig. 5b). Similarly the Nusselt number is more influenced by the cell size in the low porosity gyroid, with relative errors higher than 15% at high cell sizes A pressure drop difference less than 1% and a Nusselt number difference less than 5% were adopted as the criteria for the definition of the mesh size. As a result, a mesh dimension of 15% of ϕ_{min} was found suitable for the automatic generation of the grid of all gyroids in the STAR-CCM+ environment. To better capture the fluid velocity gradient that forms in the boundary layer near the non-slip wall, 10 prism layers were added during automatic grid generation. These layers had a total thickness equal to 20% of the base size and a stretching factor equal to 1.5. The influence between the solid region mesh and the thermal simulations was found to be negligible, a mesh dimension of 0.25 mm was selected for all the gyroids. An example of a part of the total generated mesh is depicted in the top left corner of Fig. 6 along with the cell quality distribution for both the solid and fluid mesh. For a better readability the mesh is taken considering only half of a single elementary cell, cut in the half plane orthogonal to the y-axis. The cell quality distribution plot, on the contrary, considers all the generated mesh. The cell quality is a mesh metric calculated inside the software that evaluates the suitability of each computational cell for accurate numerical gradient calculation. It combines Gauss' theorem and least-squares methods, and therefore depends on both the geometric shape of the cell, and the relative distribution of neighboring cell centroids. Low cell quality cells are usually non-orthogonal, highly flattened or with an high skewness, which may lead to inaccurate gradient evaluation and numerical instability. STAR-CCM+ guide suggests to avoid cells with a quality below 10^{-5} . The average cell quality is showed in the graph legend, with both fluid and solid meshes having a value higher than 0.5. Additionally, the solid mesh can be seen having a more homogeneous distribution of cell quality compared to the fluid region that

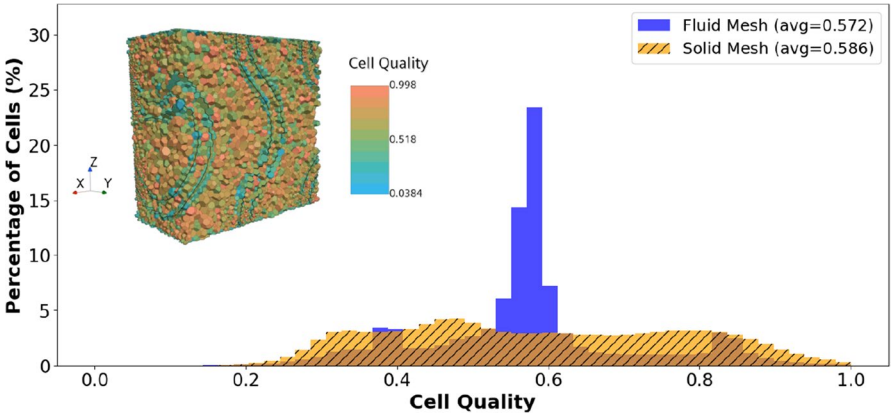

Fig. 6 Mesh quality distribution after independence study with 3D Visualization of the volumetric mesh cross section

shows a distribution peak at around 0.55. The low quality cells are located near the solid walls, due to the imposed boundary layer cells.

Velocity Field

According to Section "Proposed Approach", each gyroid was studied imposing the mass flow rate and calculating the pressure and velocity fields inside the domain. The temperature field was neglected during this investigation. The results obtained for three gyroids with cell dimensions of 10 mm and wall thickness of 0.5, 1.5 and 3 mm are shown as examples in Figs. 7 and 8. These represent the three general conditions identified in the study:

- Gyroid with larger channel diameter and higher porosity value.
- Gyroid with a medium-sized channel.
- Gyroid with a thick wall that causes the channel to collapse in on itself, generating three nearly distinct helical channels.

The results suggest that the fully developed three-dimensional flow inside the gyroid has axial and circumferential components. The axial flow originates from the imposed mass flow directed along the x-axis. At the same time, the wall thickness influences the circumferential flow component, which ultimately leads to the spiral motion seen when the channel collapses on itself as in Fig. 7c.

The details are clearer in Fig. 8, which shows the tangential velocity vector field in three planes: y/L = 1/4, y/L = 1/2 and y/L = 3/4, where L is the edge dimension.

As expected, by decreasing the ϕ_{min}, the velocity magnitude increases. This is not true in the case of the plane at y/L = 1/2, which represents the plane that cuts the cell in half, where the fluid inside the gyroid with the lower porosity is almost still. This can be explained by the specific velocity field described previously. Increasing the wall thickness leads to a complete separation of the fluid in 3 helices. For the three cases, the planes y/L = 1/4 and 3/4 represent the planes of maximum fluid propaga-

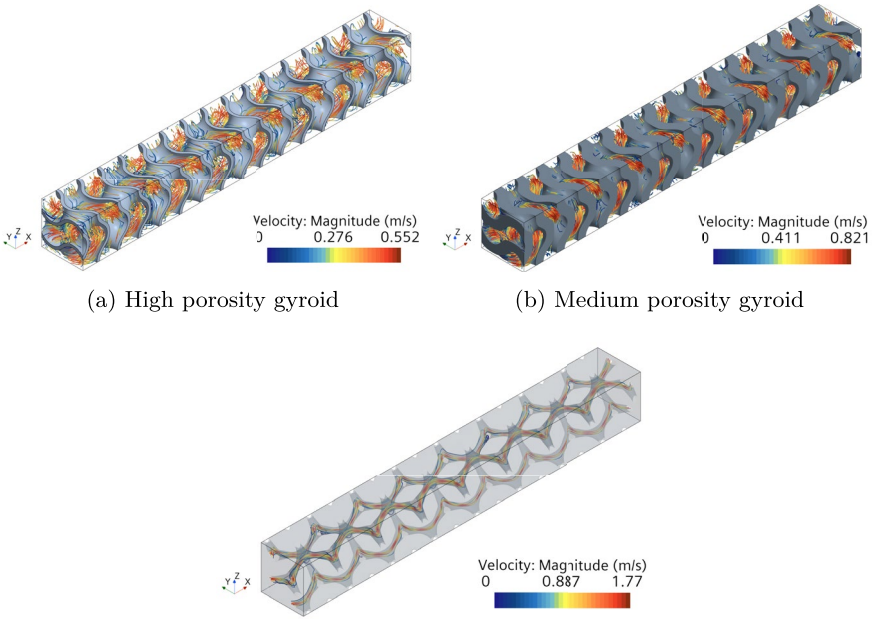

(a) High porosity gyroid (b) Medium porosity gyroid

(c) Low porosity gyroid

Fig. 7 Fluid flow streamlines obtained at imposed $Re_{\phi_{min}} = 50$ colored by velocity magnitude

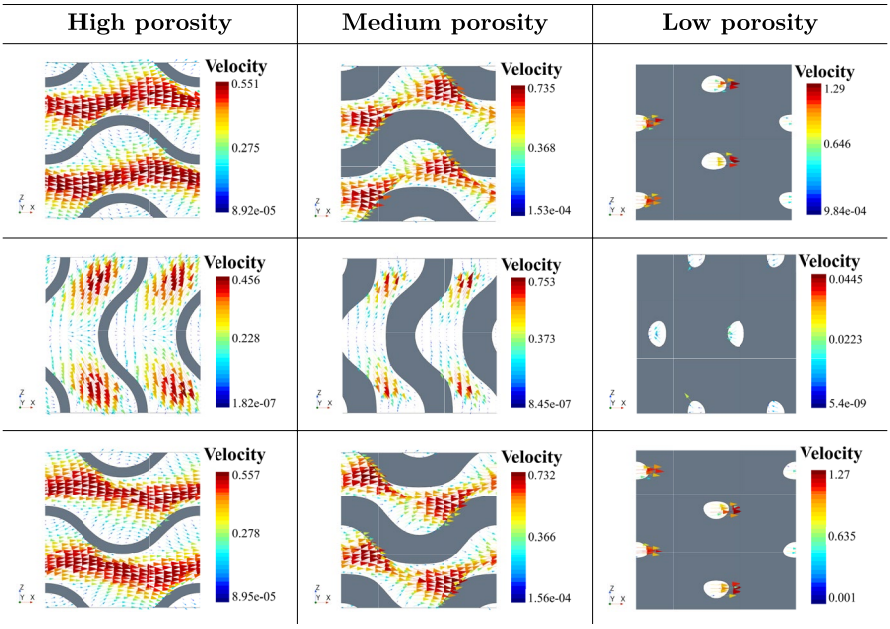

Fig. 8 Tangential velocity field (measured in m/s) on three planes y/L = 1/4 (top row), y/L = 1/2 (middle row) and y/L = 3/4 (bottom row) for three characteristic gyroids with different porosity

tion along the x-axis as the gyroid's walls align with the streamline direction and the vectors are mostly parallel to the x-axis.

Pressure Drop

At each given mass flow rate imposed in the fully developed interface, the pressure inside the domain is computed and the pressure drop between the inlet and the outlet is calculated. As stated in Section "Proposed Approach" the pressure drop is related to the specific geometry of the porous media and can be plotted against the Reynolds number. The results of the pressure drop analysis have been correlated with the two parameters used for the definition of gyroids. Figure 9a shows the comparison between different gyroids with the same wall thickness (1.5 mm), the markers are the same as Table 5, while Fig. 9b shows the correlation between pressure drop and wall thickness for gyroids with a 10 mm edge dimension.

As expected, all gyroids follow a quadratic trend. Increasing the channel dimension leads to a higher porosity, and therefore a lower pressure drop at the same Reynolds number. Keeping the same edge dimension, an increase in pressure drop is associated with an increase in wall thickness. This is particularly visible when the low porosity condition is achieved. In Fig. 9b the gyroid with 3 mm wall thickness has a pressure drop of one order of magnitude larger than in the other cases, probably caused by the geometry of specific helices that obstruct the velocity field, as previously shown. From the pressure drop, the Darcy–Weisbach friction coefficient can be calculated for each gyroid using Eq. 9 and plotted against the porosity at a fixed $Re_{\phi_{min}}$, as shown in Fig. 10 for $Re_{\phi_{min}} = 50$. At a fixed $Re_{\phi_{min}}$ the friction factor f is observed to depend primarily on porosity, reaching its maximum value when φ is approximately 50%. To verify the validity of the proposed method, the viscous and inertial resistance coefficients (R_v and R_i in Eq. 8) were calculated. The coefficient of determination R^2 was greater than 0.95 in all cases; therefore, the quadratic model described was confirmed to be accurate. The global trend of the two coefficients is shown in Fig. 11. The inertial resistance coefficient (Fig. 11a) shows a non-monotonic dependence on porosity, with a maximum around 45% for most geometries, except for the smallest cell size. To better highlight this behavior, the plot includes

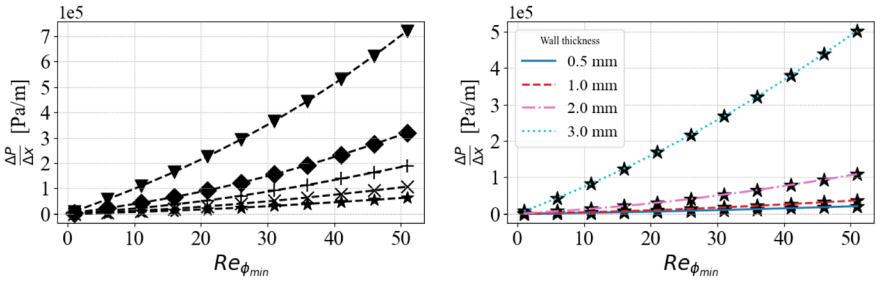

(a) 1.5 mm wall thickness (b) 10 mm edge dimension

Fig. 9 Normalized pressure drop against Reynold number for different gyroids with **a**) different edge dimension at fixed wall thickness and **b**) different wall thickness at fixed edge dimension

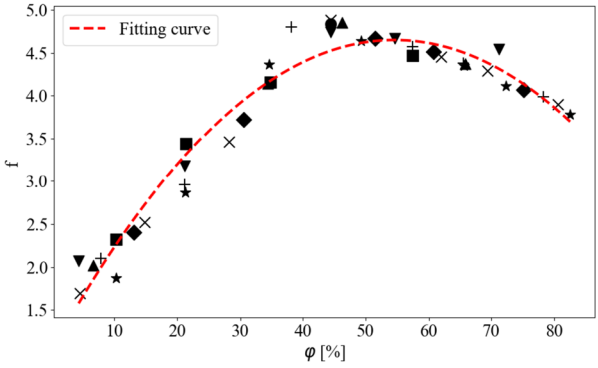

Fig. 10 Darcy–Weisbach friction factor against porosity with trend line

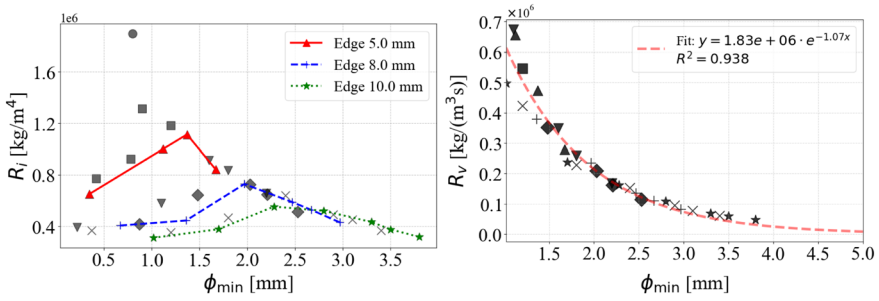

(a) Inertial Resistance (b) Viscous Resistance

Fig. 11 Porous resistance coefficients against channel dimension

three lines connecting data points from three gyroid families with edge lengths of 4, 8, and 10 mm. These trends indicate that increasing the cell size leads to a progressive flattening of the peak and a reduction in the inertial resistance, which decreases by approximately 65% when moving from a 4 mm to a 10 mm edge length gyroid. The maximum at intermediate porosity reflects the competition between enhanced flow acceleration through pore constrictions and the reduction of solid–fluid interactions at higher porosity. As the dimension of the edge increases, the permeability K of the gyroid increases, leading to a lower value of R_i. The viscous resistance coefficient is shown in Fig. 11b and follows a monotonous trend, as expected. The fluid experiences a higher resistance to the flow (high R_v) when the channel is smaller and the wall thickness increases. By combining the results of both coefficients, it can be seen that for an extremely low value of porosity, R_i is negligible with respect to R_v and the normalized pressure drop varies almost linearly with velocity. For higher porosity, instead, the two parameters assume comparable values and the normalized pressure drop follows the quadratic trend.

From R_i and R_v is it possible to calculate the permeability based Reynolds number defined in Eq. 21 and the friction factor described in Eq. 20 It can be concluded that there is a significant agreement between the results of the friction factor obtained using the suggested method and the friction factor calculated using the Forchheimer equation from literature by the graphs of Fig. 12.

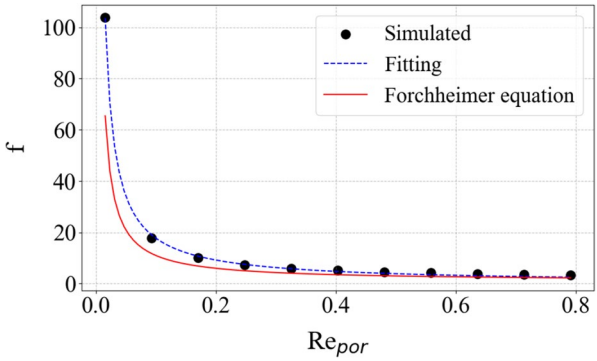

Fig. 12 Comparison between Forchheimer equation and simulated friction factor at different Re_{por}

Thermal Simulations

Following Section "Proposed Approach", after the calculation of the velocity and pressure field, by applying a generic inward heat flux it's possible to obtain a characteristic temperature field. This temperature field is independent of the heat flux applied and can be used to characterize the thermal performance of the cell. The Nusselt number becomes periodic inside the gyroid, with an average value depending on the specific geometry at a given Reynolds number. During this study, since all properties of the fluid are considered constant, hydraulic performance is not affected by the temperature field, making it possible to resolve only Eqs. 10 and 11 for a fixed velocity and pressure fields.

Temperature Field

The scaled temperature field is displayed Fig. 13 for the high, medium, and low porosity gyroids. Similarly to the vector field, the periodicity of the gyroid structure allows focusing on a single cell, which is representative of the thermal behavior of the entire structure. The temperature field obtained for gyroids with high and medium porosity is very similar, with the highest temperature occurring in the 1/4 and 3/4 y/L planes and localized close to the walls. Furthermore, by comparing these results with the velocity field shown in Fig. 8 it is possible to establish a correlation between the regions with higher temperature and those with lower velocity fields. However, the gyroid with lower porosity exhibits localized heating in the middle plane, where a higher maximum temperature is reached. Figure 13 illustrates how the fluid heats through conduction in this plane because the velocity is nearly zero, resulting in an extremely homogeneous condition.

Nusselt Number

Since the gyroid structure is periodic, the thermal efficiency will likewise be periodic after it reaches the stationary condition. By creating several cross-sections on the x-axis it is possible to plot the trend against the normalized x position against the edge length. As shown in Fig. 14 for each elementary cell the Nusselt number repeats

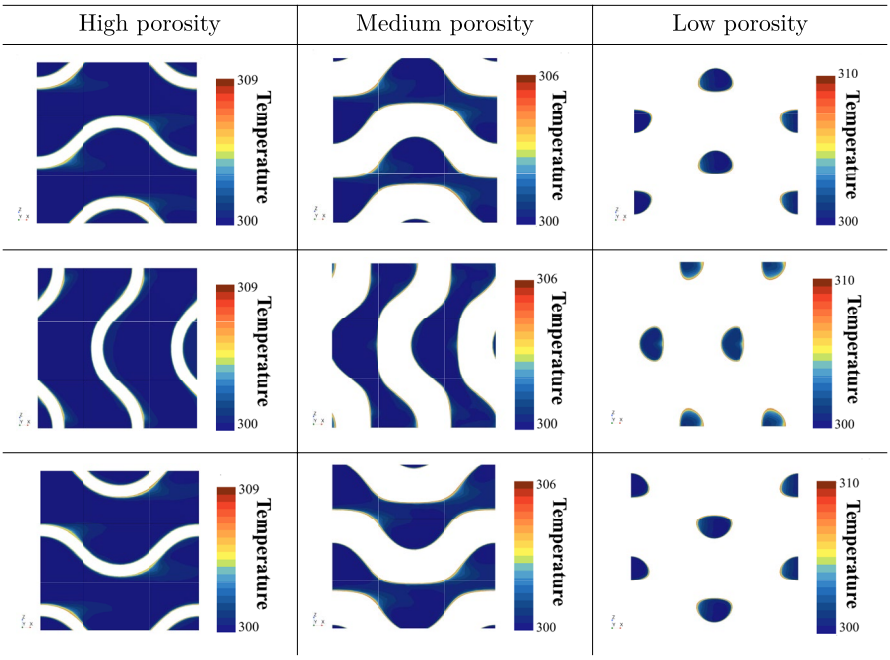

Fig. 13 Scaled temperature field (measured in K) of the fluid region on three planes y/L = 1/4 (top row), y/L = 1/2 (middle row) and y/L = 3/4 (bottom row) for three characteristic gyroids

Fig. 14 Nusselt number against normalized x for two different gyroids

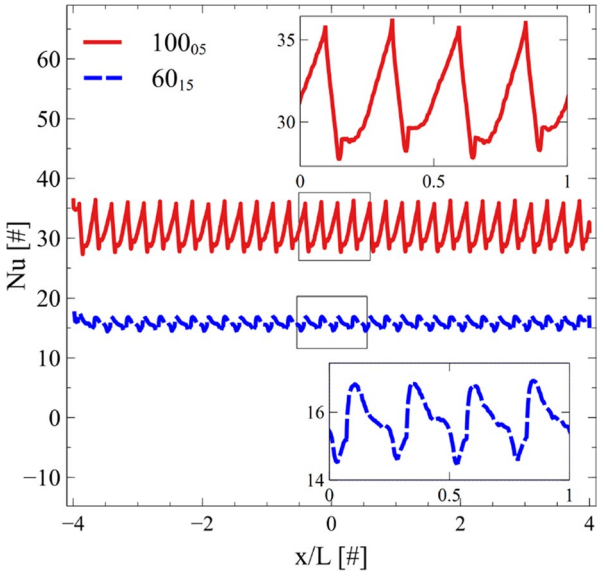

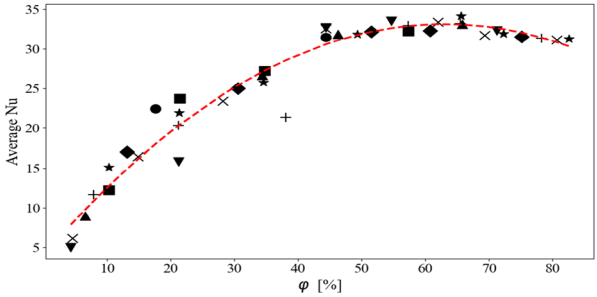

Fig. 15 Average Nusselt number at $Re_{\phi_{min}} = 50$ against porosity with quadratic trend-line

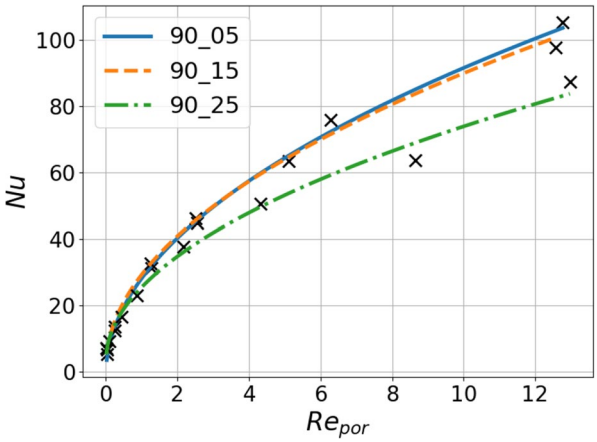

Fig. 16 Average Nusselt number against Re_{por} for three different gyroids having porosity 0.8, 0.44, and 0.15

4 times independently of the geometry itself, particularly cell 100_{05} in continuous line and cell 60_{15} in dashed line.

Consequently, the average value of the Nu number can be calculated. Figure 15 shows the average Nusselt number of all the gyroids considered against the porosity. The average Nusselt number increases as the wall thickness decreases until it reaches an almost asymptotic value. This value, for $Re_{\phi_{min}} = 50$, is reached when the porosity is higher than 40%, and it is between 30 and 35 (Fig. 15). It can be seen that different cells with similar porosity value, for example 50_{05} and 100_{10} having 65.8 % and 65.6% respectively, share a similar Nusselt number, 33.14 against 34.16 By calculating the average Nusselt number at various Re_{por} numbers it is possible to obtain a simple relationship, similar to the one used for estimating the friction factor (Eq. 20) that can be helpful during design of experiments to choose the optimal TPMS cell An example of the Nusselt number against Re_{por} for three different gyroids, specifically 90_{05}, 90_{15} and 90_{25}, is shown in Fig. 16. The following relationship is proposed:

$$Nu_{\phi_{min}} \approx A \cdot \sqrt{Re_{por}} \quad , \quad A = f(\varphi) \tag{22}$$

where A is a function of the type of TPMS geometry and porosity. In our investigation a value of A = 23.44 + 7.5 $\cdot\varphi$ was found the best fit, however, a constant value of 27.2 was even found to be highly accurate for gyroids 90_{05} and 90_{15} with a root

mean square error of 3.45 and 3.68 respectively. For gyroid 90_{25} the constant A value led to a higher RMSE equal to 7.5. The proposed method was then applied to a reference example found in literature [19] that used a traditional approach to characterize a gyroid based heat exchanger. All the input was taken from the article, including the gyroid unit cell dimension but, instead of relying on the 3D geometry used in the study, our fully developed approach was applied. Their study reported a Nusselt number ranging between 60 and 65 for a gyroid heat exchanger at $Re = 993$ (corresponding to a volumetric flow rate of 15.7 cm^3/s) using a water-ethylene glycol mixture with $Pr = 14$. Under similar geometric and fluid conditions, our numerical framework predicted an average value of 57.06 with a standard deviation of 3.52 This result is in excellent agreement with the experimental range, with the slight deviation being attributable to the absence of entrance and manifold effects in our fully developed periodic model.

PEC

The final thermal and fluid dynamic performance of gyroids were finally evaluated using the Performance Evaluator Criterion (PEC). PEC is plotted with the porosity in Fig. 17 for $Re_{\phi_{min}} = 50$. All the gyroids studied show a PEC higher than 1, which makes them cost-effective compared with the standard rectangular duct case. As porosity increases, the increase in the Nusselt number (Fig. 15) manages to balance the increase in friction factor (Fig. 10) leading to an overall increase in PEC.

Process Constraints

Production constraints were considered in this study. Representative examples of the printed specimens and the corresponding dimensional validation results are presented in Figs. 18 and 19. In particular, Fig. 18 shows the two distinct specimen geometries printed to evaluate the geometrical error of the holes (top part) and of the gyroid walls (bottom part).

Figure 19 shows the results of the geometrical evaluation. Features that fully satisfy the threshold defined in Section "Gyroid Case Study and LPBF Benchmarking" are included in the green area, while features close to the threshold, defined as acceptable, are highlighted in red with diagonal stripes.

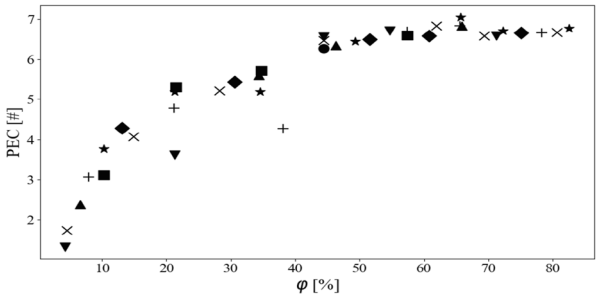

Fig. 17 Performance indicator against porosity

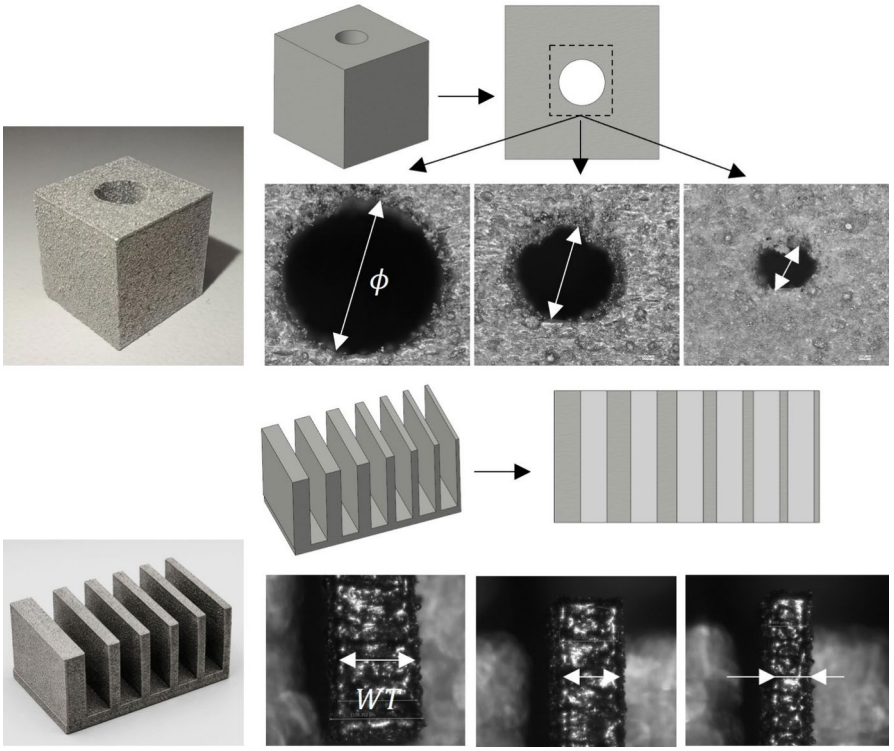

Fig. 18 3D CAD models and printed specimens used for geometrical feature evaluation

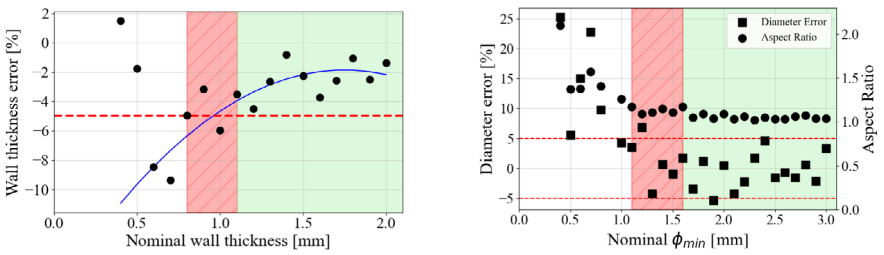

(a) Wall thickness (b) Hole diameter and aspect ratio

Fig. 19 LPBF constraints

For all samples with nominal thickness greater than 0.6 mm, the geometrical error measured on wall thickness (Fig. 19a) is negative (measured thickness lower than the nominal value), and the error decreases as the nominal thickness increases. For nominal thicknesses below 0.6 mm, the error becomes positive, indicating the minimum feature size reliably achievable by the process. However, for these thicknesses, wall planarity is compromised, and therefore these features are excluded from the acceptable range.

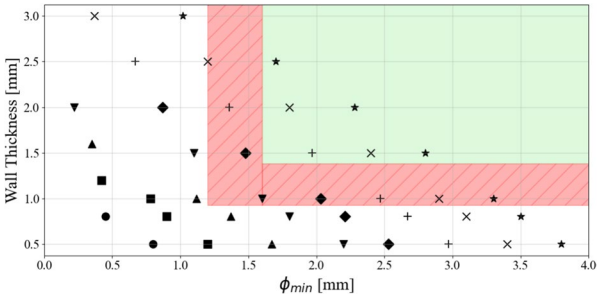

Fig. 20 Printability constraints applied to gyroid tested

Overall, nominal thickness values greater than 1.1 mm fall within the green LPBF process window, while thicknesses in the range of 0.8–1.1 mm belong to the acceptable (red) region.

Figure 19b reports the results obtained for the hole diameter evaluation. The geometrical error remains within $\pm 5\%$ for diameters larger than 1.2 mm, and the aspect ratio reaches an asymptotic value of 1.06 ± 0.02 for diameters greater than 1.6 mm. Accordingly, the green region includes holes with diameters larger than 1.6 mm, while acceptable values also include diameters in the range of 1.2–1.6 mm.

In summary, in Fig. 20, the geometries satisfying the constraints for both wall thickness and hole diameter are highlighted in green, while features that marginally violate one or both constraints are highlighted in red.

In the supplementary material, the PEC of each tested gyroid is reported along with the printability constraints. Although some gyroids with excessively thin walls exhibit the highest PEC values, they are not printable and therefore unsuitable for practical applications. Conversely, gyroids with very thick walls have been excluded to comply with the minimum channel size constraint. Additionally, these gyroids are not of interest as they exhibit the lowest PEC values, making them suboptimal for thermal enhancement. In our case, both 90_{15} and 100_{15} gyroids achieve the maximum PEC value of 6.5 while satisfying both printability constraints. The porosity of the former is 45%, while that of the latter is 50%, demonstrating that this range of porosity is optimal. It ensures good printability while simultaneously providing significant thermal enhancement, making these designs highly suitable for practical applications.

Conclusion

This study introduced a streamlined numerical framework based on periodic boundary conditions to characterize the thermal-hydraulic performance of Triply Periodic Minimal Surface (TPMS) structures under fully developed conditions. The main findings are summarized as follows:

- **Methodological Validation:** The proposed approach enables a focused analysis of the core region of TPMS structures, significantly reducing computational costs. The model's reliability was confirmed through comparison with experimental data from the literature [19]. For a gyroid structure at $Re = 993$, the

model predicted an average Nusselt number of 57.06 ± 3.52, showing excellent agreement with the experimental range of 60–65.

- **Hydraulic Performance:** All investigated gyroids follow a quadratic pressure drop trend, accurately described by the Darcy-Forchheimer model. Viscous and inertial resistance coefficients were derived, revealing that increasing the cell edge length from 4 mm to 10 mm reduces inertial resistance by approximately 65%, while viscous resistance dominates in low-porosity designs.
- **Thermal Efficiency:** The Nusselt number exhibits periodic behavior within the elementary cells. At $Re_{\phi_{min}} = 50$, *Nu* reaches an asymptotic range between 30 and 35 for porosities higher than 40%. A simplified correlation between the Nusselt and Forchheimer numbers was proposed to facilitate rapid design screening and optimization.
- **Optimal Design and Printability:** All investigated designs achieved a Performance Evaluation Criterion (PEC) higher than 1, indicating superior efficiency compared to traditional smooth ducts. By integrating Laser Powder Bed Fusion (LPBF) printability constraints, gyroids with a porosity range of 45–50% and edge lengths of 9–10 mm were identified as the optimal trade-off, achieving a maximum PEC of 6.5.

In conclusion, this work provides a rigorous and efficient tool for the optimization of next-generation 3D-printed heat exchangers, bridging the gap between mathematical design and practical manufacturing constraints.

Acknowledgements The authors would like to thank Chiara Gianassi for her valuable support and assistance during the revision of this work.

Author Contributions Samuele Piandoro: Writing — original draft; Methodology; Software; Formal analysis; Visualization; Investigation. Filippo Azzini: Writing — original draft; Methodology; Software; Formal analysis; Conceptualization; Investigation. Michele Francioso: Writing — original draft; Visualization; Investigation. Dexiang Zha: Investigation. Erica Liverani: Formal analysis; Conceptualization; Visualization; Resources. Beatrice Pulvirenti: Conceptualization; Supervision; Resources. Alessandro Fortunato: Conceptualization; Supervision; Resources. All authors reviewed and approved the final manuscript.

Funding Open access funding provided by Alma Mater Studiorum - Università di Bologna within the CRUI-CARE Agreement. The authors declare that no funds, grants, or other support were received during the preparation of this manuscript.

Data Availability The datasets generated and analyzed during the current study are available from the corresponding author on reasonable request.

Declarations

Competing Interests The authors declare no competing interests.

Ethical Approval Not applicable

References

1. Murshed, S.S., De Castro, C.: A critical review of traditional and emerging techniques and fluids for electronics cooling. Renew. Sustain. Energy Rev. **78**, 821–833 (2017)
2. Careri, F., Khan, R.H.U., Todd, C., Attallah, M.M.: Additive manufacturing of heat exchangers in aerospace applications: a review. Appl. Ther. Eng. **235**, 121387 (2023). https://doi.org/10.1016/j.applthermaleng.2023.121387
3. International Energy Agency: Electricity Market Report. OECD Publishing, Paris (2020). https://doi.org/10.1787/f0aed4e6-en, https://www.oecd-ilibrary.org/content/publication/f0aed4e6-en
4. Venkata Rao, R., Saroj, A., Ocłoń, P., Taler, J.: Design optimization of heat exchangers with advanced optimization techniques: A review. Archives of Computational Methods in Engineering **27** (2019). https://doi.org/10.1007/s11831-019-09318-y
5. Solaimani, S., Parandian, A., Nabiollahi, N.: A holistic view on sustainability in additive and subtractive manufacturing: A comparative empirical study of eyewear production systems. Sustainability **13**(19) (2021). https://doi.org/10.3390/su131910775
6. Jafari, D., Wits, W.W.: The utilization of selective laser melting technology on heat transfer devices for thermal energy conversion applications: A review. Renew. Sustain. Energy Rev. **91**, 420–442 (2018). https://doi.org/10.1016/j.rser.2018.03.109
7. Kaur, I., Singh, P.: State-of-the-art in heat exchanger additive manufacturing. Int. J. Heat Mass Transf. **178**, 121600 (2021). https://doi.org/10.1016/j.ijheatmasstransfer.2021.121600
8. Narsimhachary, D., Kalyan, P.M.: Additive manufacturing: Environmental impact, and future perspective. In: Practical Implementations of Additive Manufacturing Technologies, pp. 295–308. Springer, Cham (2023). Chap. 14
9. Frazier, W.E.: Metal additive manufacturing: a review. J. Mater. Eng. Perform. **23**, 1917–1928 (2014)
10. Feng, J., Fu, J., Yao, X., He, Y.: Triply periodic minimal surface (tpms) porous structures: From multi-scale design, precise additive manufacturing to multidisciplinary applications. Int. J. Extreme Manuf. **4**(2) (2022). https://doi.org/10.1088/2631-7990/ac5be6
11. Pulvirenti, B., Celli, M., Barletta, A.: Flow and convection in metal foams: A survey and new cfd results. Fluids **5**(3), 155 (2020)
12. Karcher, H., Polthier, K.: Construction of triply periodic minimal surfaces. Philosophical Transactions of the Royal Society of London. Series A: Mathematical, Physical and Engineering Sciences **354**(1715), 2077–2104 (1996)
13. Khan, N., Riccio, A.: A systematic review of design for additive manufacturing of aerospace lattice structures: Current trends and future directions. Progress in Aerospace Sciences **149**, 101021 (2024). https://doi.org/10.1016/j.paerosci.2024.101021
14. Ormiston, S., Srinivas Sundarram, S.: Fiberglass-reinforced triply periodic minimal surfaces (tpms) lattice structures for energy absorption applications. Polym. Compos. **45**(1), 523–534 (2024). https://doi.org/10.1002/pc.27795
15. Jones, A., Leary, M., Bateman, S., Easton, M.: Tpms designer: A tool for generating and analyzing triply periodic minimal surfaces. Software Impacts **10**, 100167 (2021). https://doi.org/10.1016/j.simpa.2021.100167
16. Khalil, M., Hassan Ali, M.I., Khan, K.A., Abu Al-Rub, R.: Forced convection heat transfer in heat sinks with topologies based on triply periodic minimal surfaces. Case Studies in Thermal Engineering **38**, 102313 (2022). https://doi.org/10.1016/j.csite.2022.102313

17. Wang, J., Chen, K., Zeng, M., Ma, T., Wang, Q., Cheng, Z.: Investigation on flow and heat transfer in various channels based on triply periodic minimal surfaces (tpms). Energy Convers. Manage. **283**, 116955 (2023). https://doi.org/10.1016/j.enconman.2023.116955
18. Baobaid, N., Ali, M.I., Khan, K.A., Abu Al-Rub, R.K.: Fluid flow and heat transfer of porous tpms architected heat sinks in free convection environment. Case Studies in Thermal Engineering **33**, 101944 (2022). https://doi.org/10.1016/j.csite.2022.101944
19. Saghir, M.Z., Yahya, M., Ortiz, P.D., Impellizzeri, S., Al-Ketan, O.: Heat enhancement of ethylene glycol/water mixture in the presence of gyroid tpms structure: Experimental and numerical comparison. Processes **13**(1) (2025). https://doi.org/10.3390/pr13010228
20. Dukhan, N., Patel, K.P.: Entrance and exit effects for fluid flow in metal foam. AIP Conf. Proc. **1254**(1), 299–304 (2010). https://doi.org/10.1063/1.3453828, https://pubs.aip.org/aip/acp/article-pdf/1254/1/299/11588593/299_1_online.pdf
21. Baril, E., Mostafid, A., Lefebvre, L.-P., Medraj, M.: Experimental demonstration of entrance/exit effects on the permeability measurements of porous materials. Adv. Eng. Mater. **10**(9), 889–894 (2008). https://doi.org/10.1002/adem.200800142, https://onlinelibrary.wiley.com/doi/pdf/10.1002/adem.200800142
22. Nowak, R.: Estimation of viscous and inertial resistance coefficients for various heat sink configurations. Procedia Engineering **157**, 122–130 (2016). https://doi.org/10.1016/j.proeng.2016.08.347 . Selected Papers from IX International Conference on Computational Heat and Mass Transfer (ICCHMT2016)
23. Schoen, A.H.: Infinite periodic minimal surfaces without self-intersections. Technical Report NASA TN D-5541, National Aeronautics and Space Administration, Washington, DC (1970)
24. nTopology Inc: nTop (2023). https://ntop.com
25. Renon, C., Jeanningros, X.: A numerical investigation of heat transfer and pressure drop correlations in gyroid and diamond tpms-based heat exchanger channels. Int. J. Heat Mass Transf. **239**, 126599 (2025). https://doi.org/10.1016/j.ijheatmasstransfer.2024.126599
26. Nield, D.A., Bejan, A.: Convection in Porous Media, 4th edn. Springer, New York, NY (2017). https://doi.org/10.1007/978-3-319-49562-0
27. Bonnet, J.-P., Topin, F., Tadrist, L.: Flow laws in metal foams: compressibility and pore size effects. Transp. Porous Media **73**(2), 233–254 (2008)
28. Everts, M., Meyer, J.P.: Laminar hydrodynamic and thermal entrance lengths for simultaneously hydrodynamically and thermally developing forced and mixed convective flows in horizontal tubes. Exp. Thermal Fluid Sci. **118**, 110153 (2020). https://doi.org/10.1016/j.expthermflusci.2020.110153
29. Zimparov, V.D., Vulchanov, N.L.: Performance evaluation criteria for enhanced heat transfer surfaces. Int. J. Heat Mass Transf. **37**(12), 1807–1816 (1994). https://doi.org/10.1016/0017-9310(94)90069-8
30. Webb, R.L.: Performance evaluation criteria for use of enhanced heat transfer surfaces in heat exchanger design. Int. J. Heat Mass Transf. **24**(4), 715–726 (1981). https://doi.org/10.1016/0017-9310(81)90015-6
31. Shah, R.K., London, A.L.: Chapter vii - rectangular ducts. In: Shah, R.K., London, A.L. (eds.) Laminar Flow Forced Convection in Ducts, pp. 196–222. Academic Press, New York (1978). https://doi.org/10.1016/B978-0-12-020051-1.50012-7, https://www.sciencedirect.com/science/article/pii/B9780120200511500127
32. Schindelin, J., Arganda-Carreras, I., Frise, E., Kaynig, V., Longair, M., Pietzsch, T., Preibisch, S., Rueden, C., Saalfeld, S., Schmid, B., Tinevez, J.-Y., White, D.J., Hartenstein, V., Eliceiri, K., Tomancak, P., Cardona, A.: Fiji: an open-source platform for biological-image analysis. Nat. Methods **9**(7), 676–682 (2012)
33. American Society of Heating: Refrigerating and Air-Conditioning Engineers (ASHRAE): ASHRAE Handbook — Fundamentals. American Society of Heating, Refrigerating and Air-Conditioning Engineers (ASHRAE), Atlanta, GA, USA (2017)
34. Touloukian, Y.S., Powell, R.W., Ho, C.Y., Klemens, P.G.: Thermal Conductivity: Metallic Elements and Alloys. Thermophysical Properties of Matter, vol. 1. IFI/Plenum, New York, NY, USA (1970)
35. Moradmand, M.M., Sohankar, A.: Numerical and experimental investigations on the thermal-hydraulic performance of heat exchangers with schwarz-p and gyroid structures. Int. J. Therm. Sci. **197**, 108748 (2024). https://doi.org/10.1016/j.ijthermalsci.2023.108748

Authors and Affiliations

Samuele Piandoro[1] · Filippo Azzini[1] · Michele Francioso[1] · Dexiang Zha[1] · Erica Liverani[1] · Beatrice Pulvirenti[1] · Alessandro Fortunato[1]

✉ Samuele Piandoro
samuele.piandoro2@unibo.it

Filippo Azzini
filippo.azzini2@unibo.it

Michele Francioso
michele.francioso2@unibo.it

Dexiang Zha
dexiang.zha2@unibo.it

Erica Liverani
erica.liverani2@unibo.it

Beatrice Pulvirenti
beatrice.pulvirenti@unibo.it

Alessandro Fortunato
alessandro.fortunato@unibo.it

[1] Department of Industrial Engineering, Alma Mater Studiorum University of Bologna, Viale Risorgimento 2, Bologna 40136, Italy